







**Electronic states and quantum transport in bilayer graphene Sierpinski-carpet fractals**Xiaotian Yang <sup>1</sup>, Weiqing Zhou <sup>2</sup>, Qi Yao <sup>3</sup>, Yunhai Li <sup>1</sup>, Yunhua Wang <sup>1,4,\*</sup> and Shengjun Yuan <sup>1,5,†</sup><sup>1</sup>Key Laboratory of Artificial Micro- and Nano-structures of Ministry of Education and School of Physics and Technology, *Wuhan University*, Wuhan 430072, China<sup>2</sup>AI for Science Institute, Beijing 100080, China<sup>3</sup>Quantum Science Center of Guangdong-Hongkong-Macao Greater Bay Area (Guangdong), Shenzhen 518045, China<sup>4</sup>Lanzhou Center of Theoretical Physics and Key Laboratory for Quantum Theory and Applications of the Ministry of Education and Key Laboratory of Theoretical Physics of Gansu Province and School of Physical Science and Technology, *Lanzhou University*, Lanzhou 730000, China<sup>5</sup>Wuhan Institute of Quantum Technology, Wuhan 430206, China

(Received 17 April 2024; revised 6 June 2024; accepted 11 June 2024; published 21 June 2024)

We construct Sierpinski carpets (SCs) based on AA or AB bilayer graphene using atom vacancies, which we denote SC-AA and SC-AB, to investigate the effects of interlayer coupling on the electronic properties of fractals. Compared with monolayer graphene SCs, their densities of states have similar features, such as Van Hove singularities and edge states corresponding to the central peaks near zero energy, but remarkable energy broadening of edge states emerges in SC-AA and SC-AB. The calculated conductance spectrum shows that the conductance fluctuations still retain the Hausdorff fractal dimension behavior even with the interlayer coupling. Thus, the high correlation between quantum conductance and the fractal geometry dimension is not affected by the interlayer coupling in bilayer graphene SCs. We further reveal the quasieigenstates in fractal-like pressure-modulated bilayer graphene, denote SC-pAA and SC-pAB. Numerical results show that the density of states of SC-pAA (SC-pAB) shows an asymptotic behavior compared to that of SC-AA (SC-AB), especially for high-energy quasieigenstates. Within a certain energy range, stronger pressure can lead to stronger localization, forming an efficient fractal space.

DOI: [10.1103/PhysRevB.109.235429](https://doi.org/10.1103/PhysRevB.109.235429)**I. INTRODUCTION**

A fractal is a unique structure with fascinating self-similarity and a noninteger Hausdorff dimension  $d_H$  [1–4]. The two intrinsic characteristics of this unconventional system enable exotic and interesting physical features in electronic energy spectrum statistics [5–9], quantum transport [10–16], plasmons [17], flat bands [18–21], topological phases [22–29], enhanced superconductivity [30], and the modified superarea law of entanglement entropy [31]. Experimentally, nanoscale fractals, such as Sierpinski carpets (SCs) and Sierpinski gaskets, are mainly created using bottom-up nanofabrication methods, including molecular self-assembly [32–38], chemical reactions [39], template packing [40], and atomic manipulations in a scanning tunneling microscope [41–43]. Recently, SC photonic lattices were also created to investigate photon evolution [44]. Top-down external field modulation is another feasible method for generating large-scale fractal structures. Especially, the graphene lattice can much more easily form an effective fractional dimension with a small electric field compared with square lattice materials [11]. In addition, there are some unique physical properties in graphene fractal systems. For instance, the geometry

dimension of a monolayer graphene SC is characterized by quantum conductance fluctuations [10,11]. In addition, the eigenstates of graphene fractals exhibit various localized distributions in real space, and the edge states induced by zigzag terminations are localized at the hole boundaries of the graphene SC, forming a special state distribution [11]. In functionalized graphene SCs, there are two special energy windows where holes are mainly located inside the functionalized region and electrons are mainly located inside the fractal region [12].

Different from the electronic structure of monolayer graphene, bilayer graphene with AA or AB stacking has a parabolic dispersion in the low-energy range owing to interlayer coupling. Recent theoretical calculations and experimental research showed that external vertical pressure can enhance the interlayer coupling and change the physical properties of few-layer graphene, such as the electronic structure [45–49], Raman spectrum [48–51], magnetism [52–54], phase transition [54–56], and superconductivity [57]. Especially, it has been proved that the interlayer interactions in certain regions can be controlled by locally modifying the interlayer separation by applying pressure from a scanning tunneling microscopy tip [47]. As a natural extension of graphene fractals, we want to know how the electronic states and quantum transports are in bilayer graphene Sierpinski-carpet fractals formed by atom vacancies, which we denote SC-AA and SC-AB. Owing to the high tunability of the interlayer

\*Contact author: wangyunhua@lzu.edu.cn

†Contact author: s.yuan@whu.edu.cn

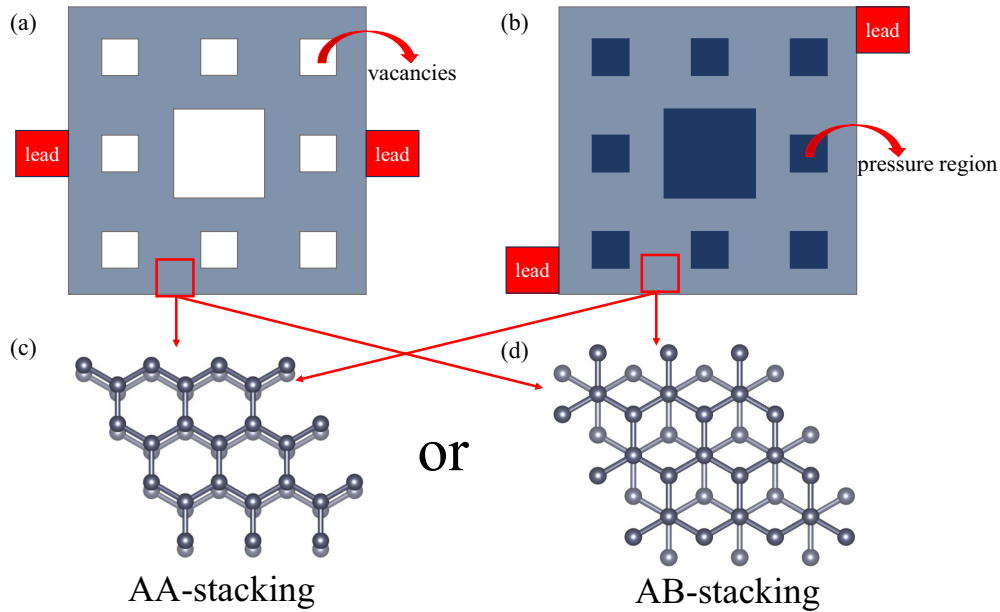


FIG. 1. (a) Schematic diagram of an AA- or AB-stacked graphene SC sample generated by atom vacancies with iteration number  $I = 2$  and square width  $W = 32.5a$ , with  $a$  being the lattice constant of graphene. (b) Schematic diagram of an AA- or AB-stacked graphene SC sample generated by local pressure modulations. Here, the dark region is called area II (pressure region), and the light region is called area I (fractal space). The atomic structures of AA- and AB-stacked bilayer graphene are shown in (c) and (d), respectively. Different position configurations of the leads, called central and diagonal leads, are applied to the sample for calculations of quantum conductance.

coupling by pressure, we further want to ask what the electronic states are like in fractal-like pressure-modulated AA and AB bilayer graphene (denoted SC-pAA and SC-pAB, respectively) and what the difference is among the four types of bilayer graphene fractals.

In this work, we investigate the electronic states and quantum conductance fluctuations in SC-AA and SC-AB. Remarkable energy broadening of quasieigenstates around zero energy as edge states is observed in the calculated results for the density of states (DOS) and real-space distributions of the probability density. The quantum conductance fluctuations keep the Hausdorff fractal dimension behavior similar to that of monolayer graphene fractals, even in the presence of inter-layer coupling in bilayer graphene fractals. We also reveal the electronic states in pressure-modulated bilayer graphene fractals, including the SC-pAA and SC-pAB structures. The DOS results for SC-pAA (SC-pAB), especially for high-energy quasieigenstates, show behavior asymptotic to that of SC-AA (SC-AB) as pressure increases. Our analyses of real-space distributions of the normalized probability density also verify the DOS results. Moreover, within a certain pressure range, stronger pressure can lead to stronger localization, forming a more efficient fractal space in SC-pAA and SC-pAB. However, even for these high-energy quasieigenstates, their DOS in SC-pAA (SC-pAB) cannot exactly replicate the same spectrum as SC-AA (SC-AB) within the experimental pressure range.

This paper is organized as follows. In Sec. II, we describe the tight-binding model and provide the details of the applied numerical methods. In Sec. III, we perform the calculations and show the results for electronic properties and quantum transport for SC-AA, SC-AB, SC-pAA, and SC-pAB,

including the density of states, quasieigenstates, quantum conductance, and box-counting analysis of the conductance fluctuation. A brief summary is given in Sec. IV.

## II. MODEL AND METHODS

We investigate two types of bilayer graphene SC structures: (1) the first type is generated by atom vacancies, as shown in Figs. 1(a), and (2) the second type is formed by external pressure modulation, as depicted in Fig. 1(b). For convenience, we label the AA- (AB-) stacked graphene SC formed by atom vacancies as SC-AA (SC-AB) and the AA- (AB-) stacked graphene SC with pressure as SC-pAA (SC-pAB). The structural parameters used in Fig. 1 are listed here.  $I = 2$  is the iteration number, and  $W = 32.5a$  is the sample width, with  $a = 2.46 \text{ \AA}$  being the lattice constant of graphene. When SC changes from the  $I$ th iteration to the  $(I + 1)$ th iteration, the unit is replicated with an  $\mathcal{N} = 8$  times larger area and  $\mathcal{L} = 3$  times larger width. The Hausdorff dimension is defined as  $d_H \equiv \log_{\mathcal{L}} \mathcal{N} \simeq 1.89$ .

The behaviors of electrons and holes in these SC systems are governed by the following tight-binding Hamiltonian:

$$H = - \sum_{\alpha} \sum_{i,j} t_{\alpha,ij} c_i^{\dagger} c_j + \sum_i \varepsilon_i c_i^{\dagger} c_i, \quad (1)$$

where  $\varepsilon_i$  is the on-site energy at the  $i$ th site.  $c_i^{\dagger}$  and  $c_j$  are creation and annihilation operators.  $t_{ij}$  is the electron hopping between the  $i$ th and  $j$ th sites, including intralayer ( $\alpha = 0$ ) and interlayer ( $\alpha = 1$ ) hopping. This tight-binding Hamiltonian is obtained from the maximally localized Wannier orbitals [58,59]. The intralayer hopping energy up to third-nearest neighbors for the graphene monolayer has values of  $-2.8922$ ,

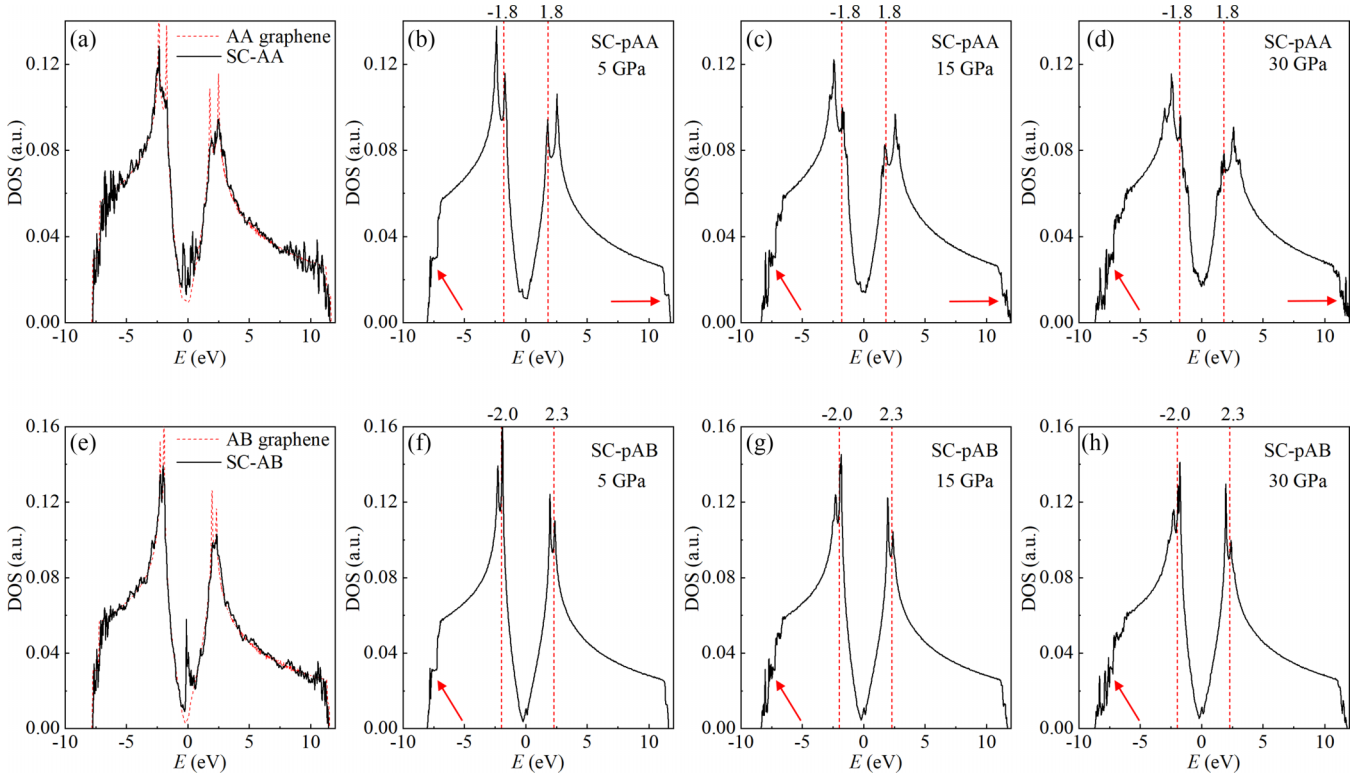


FIG. 2. DOSs of SC-AA (AB) and pristine AA- (AB-) stacked graphene are shown in (a) and (e). DOSs of SC-pAA (SC-pAB) for varying degrees of external pressure are shown for (b) and (f) 5 GPa, (c) and (g) 15 GPa, and (d) and (h) 30 GPa. The sample parameters are set as  $W = 297.5a$  and  $I = 4$ .

0.2425, and  $-0.2656$  eV, respectively. The interlayer hopping is a function of both distance and orientation [59]:

$$t_{\alpha=1,ij}(\mathbf{r}) = V_0(r) + V_3(r)[\cos(3\theta_{12} + \cos(3\theta_{21})] + V_6(r)[\cos(6\theta_{12}) + \cos(6\theta_{21})], \quad (2)$$

where the three terms originate from the different angular momenta of the wave functions.  $\mathbf{r}$  is the projection vector connecting two sites in different layers.  $r = |\mathbf{r}|$  denote the projected distances.  $\theta_{12}$  and  $\theta_{21}$  are the angles between the projected interlayer bonds and the in-plane nearest-neighbor bonds. The three radial functions involving the 10 hopping parameters in Table I are given by

TABLE I. The 10 hopping parameters in the interlayer coupling model. All values are in units of eV and take the form in Eq. (5).

$y_i$	$f_i^{(0)}$	$f_i^{(1)}$	$f_i^{(2)}$
$\lambda_0$	0.310	-1.882	7.741
$\xi_0$	1.750	-0.618	1.848
$\kappa_0$	1.990	1.007	2.427
$\lambda_3$	-0.068	0.399	-1.739
$\xi_3$	3.286	-0.914	12.011
$x_3$	0.500	0.322	0.908
$\lambda_6$	-0.008	0.046	-0.183
$\xi_6$	2.272	-0.721	-4.414
$x_6$	1.217	0.027	-0.658
$\kappa_6$	1.562	-0.371	-0.134

$$\begin{aligned} V_0(r) &= \lambda_0 e^{-\xi_0 \bar{r}^2} \cos(\kappa_0 \bar{r}), \\ V_3(r) &= \lambda_3 \bar{r}^2 e^{-\xi_3 (\bar{r}-x_3)^2}, \\ V_6(r) &= \lambda_6 e^{-\xi_6 (\bar{r}-x_6)^2} \sin(\kappa_6 \bar{r}), \end{aligned} \quad (3)$$

where  $\bar{r} = r/a$ . These formulas reflect how these radial functions rely on the projected distance and the relative angle between the interlayer vector and the monolayer plane. For bilayer graphene, the interlayer compression is related to the external pressure  $P$ . In the absence of significant reconfiguration of bilayer graphene, the pressure created by the compression from DFT calculations [60] is well fitted by the following expression as a function of the compression strain [46]:

$$P = A(e^{-B\eta} - 1), \quad (4)$$

where  $\eta$  is the magnitude of the compression strain, defined by  $\eta = \frac{h_0 - h}{h_0}$ , with  $h_0$  and  $h$  being the interlayer distances for the uncompressed and compressed cases, respectively. Here, the fitted parameters are given by  $A = 5.73$  GPa and  $B = 9.54$  [60]. The vertical compression has a weak effect on the intralayer hoppings but significantly enhances the interlayer coupling. The 10 hopping parameters involving the interlayer coupling in Eq. (3) are obtained through the following quadratic fitting [60]:

$$y_i(\eta) = f_i^{(0)} - f_i^{(1)}\eta + f_i^{(2)}\eta^2, \quad (5)$$

where  $y_i$  denotes an arbitrary choice of one of the 10 hopping parameters with the coefficients  $f_i^{(0)}$ ,  $f_i^{(1)}$ , and  $f_i^{(2)}$  listed in Table I [60].

Since numerical calculations based on exact diagonalization can treat only systems with a site number less than 10 000, we use the tight-binding propagation method (TBPM) [61] to calculate the electronic properties for a large system with millions of sites, including the density of states and quasieigenstates (see the details given in the Appendix). We start the evolution of a quantum system with a random initial state  $|\varphi(0)\rangle$ , which is a normalized superposition of all basis states  $\sum_n A_n |n\rangle$ . The DOS is calculated via Fourier transform of the correlation function [61,62]:

$$D(E) = \frac{1}{2\pi} \int_{-\infty}^{\infty} e^{iEt} \langle \varphi(0) | e^{-iHt} | \varphi(0) \rangle dt. \quad (6)$$

After the Fourier transform of states at different times during the evolution  $|\varphi(t)\rangle = e^{-iHt} |\varphi(0)\rangle$ , we obtain the quasieigenstates  $|\psi(E)\rangle$  by [61,63]

$$\begin{aligned} |\psi(E)\rangle &= \frac{1}{2\pi} \int_{-\infty}^{\infty} dt e^{iEt} |\varphi(t)\rangle \\ &= \frac{1}{2\pi} \sum_n A_n \int_{-\infty}^{\infty} dt e^{i(E-E_n)t} |n\rangle \\ &= \sum_n A_n \delta(E - E_n) |n\rangle, \end{aligned} \quad (7)$$

which can be further normalized as

$$|\psi(E)\rangle = \frac{1}{\sqrt{\sum_n |A_n|^2 \delta(E - E_n)}} \sum_n A_n \delta(E - E_n) |n\rangle. \quad (8)$$

For the finite fractal structure, one can take an average using different realizations of random coefficients  $A_n$  to obtain more accurate results for  $D(E)$  and  $|\psi(E)\rangle$ . The numerical implementation of the TBPM method is applied in TBPLAS [64], which is an open-source package [65] for building and solving tight-binding models, with an emphasis on handling large systems.

For the transport properties, we adopt the quantum transport simulator KWANT to perform the numerical calculations [66]. In KWANT, the system considered is treated as a scattering region. The scattering matrix  $S_{ij}$  and the wave function inside the scattering region  $\phi_n^S$  are the main raw output. They are calculated by matching the wave function in the lead to the wave function in the scattering region. After  $S_{ij}$  is obtained, the quantum conductance  $G_{ab} = dI_a/dV_b$  can be calculated using the Landauer formula:

$$G_{ab} = \frac{e^2}{h} \sum_{i \in a, j \in b} |S_{ij}|^2, \quad (9)$$

where  $a$  and  $b$  are two electrodes.

### III. RESULTS AND DISCUSSION

#### A. Density of states

If the iteration number of the fractal reaches a certain number, the fine structure of the fractal is completely revealed, and the distribution of electronic states changes little. Our previous numerical results [11,12] showed that the fourth iteration,  $I = 4$ , for a monolayer graphene SC is enough for the convergence of DOS calculations. The number of sites ( $\sim 410\,048$  sites) for SC-AA and SC-AB is twice that for monolayer

graphene SC, and hence, we only need to average a small number of initial states within the TBPM method to explore the electronic and transport characteristics of SC-AA and SC-AB for  $I = 4$ . The DOS of SC-AA as a function of energy is shown in Fig. 2(a). We can see that, due to the existence of the second- and third-nearest-neighbor hopping, the electron and hole states are not symmetrical in the energy spectrum. Two distinct Van Hove singularities appear around  $E = \pm 2.9$  eV, similar to those of SCs based on monolayer graphene. In fact, the DOS spectrum of pristine AA-stacked graphene exhibits four Van Hove singularities, while the formation of fractal geometry caused by atomic vacancies leads to the merging of every two adjacent Van Hove singularities into a single peak, as shown in Fig. 2(a). In addition, the central peak caused by edge states emerges due to the open boundaries. However, compared with the monolayer graphene SC [12], SC-AA exhibits an increased number of central peaks with an obvious broadening. In Fig. 2(e), similar behavior is found in the DOS for SC-AB. The energy width of the central peak in SC-AB is also significantly enlarged. Here, we have used the Fermi energy as the zero-energy reference point in the calculation.

In order to investigate the behavior of electrons in fractal-like pressure-modulated bilayer graphene, i.e., with area II under pressure, we change the external pressure and examine the change in the DOS. For SC-pAA under 5 GPa pressure, the DOS is nearly identical to that of pristine AA-stacked bilayer graphene, with its four Van Hove singularities [see Fig. 2(b)]. However, as the pressure increases, the two Van Hove points gradually get close, and some small peaks appear around zero energy. In the high-energy region, the DOS becomes more chaotic like SC-AA, as shown by the red arrows in Figs. 2(c) and 2(d). Therefore, as the applied pressure increases, the pressurized area II acts as an insulating region preventing electrons and holes from hopping from area I to area II. Naively, as the pressure grows infinitely larger, area II will gradually be isolated from the whole system, and it will act like vacancies of SC-AA, so that the DOS will be not smooth. Here, the maximum pressure applied during the DOS calculation is set to 30 GPa because there is no significant atomic restructuring of the graphene bilayer under this pressure value [60]. In experiments, the diamond-anvil cell can apply a high pressure of up to 50 GPa to a suspended graphene bilayer [67]. As shown in Figs. 2(f)–2(h), with increasing pressure, the DOS of SC-pAB also undergoes similar changes. There is a small peak at the zero-energy point of the energy spectrum, and the DOS gradually becomes chaotic in the high-energy region. However, compared with SC-pAA, SC-pAB shows relatively lower sensitivity to pressure modulation. With the increase in pressure, obvious changes in the DOS, including the broadening and splitting of peaks near the Van Hove singularities, can be observed in SC-pAA. However, in SC-pAB, even when the pressure reaches 30 GPa in Fig. 2(h), the DOS of SC-pAB still has four peaks of Van Hove singularities. Based on these results, we expect that the electronic states of SC-pAA and SC-pAB will exhibit a fractal geometric distribution in some energy ranges, which will be confirmed in following quasieigenstates (see Sec. III B). However, within the considered pressure range, it cannot exactly replicate the same spectrum as SC-AA or SC-AB because area II can be

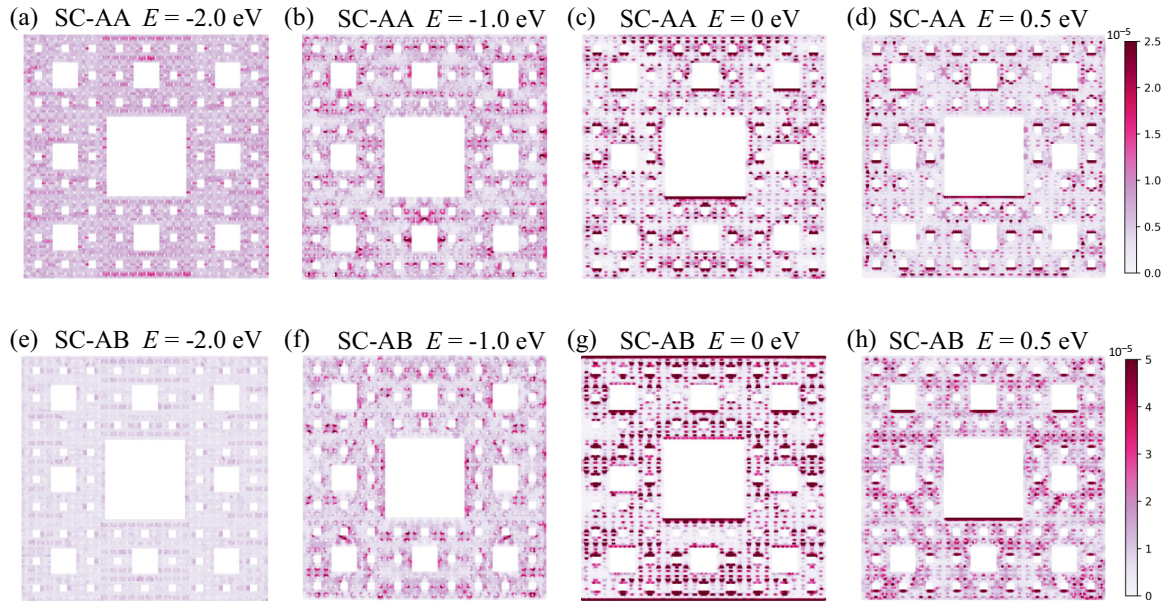


FIG. 3. The real-space distribution of quasieigenstates for SC-AA and SC-AB at (a) and (e)  $E = -2$  eV, (b) and (f)  $E = -1$  eV, (c) and (g)  $E = 0$  eV, and (d) and (h)  $E = 0.5$  eV. The sample parameters are set to  $W = 297.5a$  and  $I = 4$ .

considered to have vacancies only if the pressure is infinite. In particular, the rate of DOS change in SC-pAB with pressure modulation is significantly slower than in SC-pAA.

### B. Quasieigenstates

Using Eq. (7), we calculate the quasieigenstates of SC-AA and SC-AB and plot the real-space distributions of their probability densities in Fig. 3. We first discuss the probability density distributions of high-energy states in SC-AA, for example, the energy states at  $E = -2$  eV and  $E = -1$  eV in Figs. 3(a) and 3(b). Their nonzero probability densities are inside the fractal space (area I). Some electronic states at  $E = -2$  eV exhibit localization, and many electronic states for  $E = -1$  eV are localized at the edges of holes formed by atomic vacancies. In fact, due to the existence of atomic vacancies, electrons can be confined only in area I. For the zero-energy states in Fig. 3(c), these nonzero probability densities are obviously located at these zigzag terminations. In addition, these edge state still exist even for energy at  $E = 0.5$  eV in Fig. 3(d). This manifests the enhanced broadening of zero-energy states in bilayer graphene SCs, and it is consistent with the results for the DOS in Fig. 2(a). Therefore, the central peaks around  $E = 0$  eV in Fig. 2(a) correspond to these edge states, and such edge states are often caused by the zigzag edges of the honeycomb lattice, where atomic vacancies break lattice symmetry and induce the energy broadening. For SC-AB in Figs. 3(e) and 3(f), we can also observe similar distribution for high-energy states. The energy broadening of the central peak also increases, as shown in the Figs. 3(g) and 3(h). Compared with SC-AA, the nonzero probability densities at the Fermi energy are not only distributed at the internal lattice edge but also located at the top and bottom boundaries of the sample.

We next discuss the quasieigenstates of SC-pAA and SC-pAB under different pressures. First, we sum over the amplitudes of the normalized quasieigenstate in area I without

pressure, which can be a measure of the distributions in area I. We call this quantity the occupation percentage  $O_1$ . If  $O_1$  of area I for a given energy is 100%, the given energy state is distributed only inside area I. In this case, the electron with this energy is completely confined in the “fractal” region. On the contrary, if  $O_1$  is zero, electrons are localized inside area II; i.e., electrons have no access to any site in area I. For the bilayer graphene SC considered in this paper, the sample parameters are  $W = 297.5a$  and  $I = 4$ , and number of sites is 410 048. The number of sites in area I (area II) accounts for 62.40% (37.60%) of the entire system. If the occupation number  $O_1$  is lower than 62.40%, the electrons are mainly distributed in the pressure region. In Figs. 4(a) and 4(b), we show the calculated occupation percentage  $O_1$  of quasieigenstates under different pressures in the energy range from  $-2.5$  to  $2.5$  eV. In SC-pAA,  $O_1$  retains a high value and forms a platform with  $|E| > 1.8$  eV, which means eigenstates at the high energy are mainly distributed in area I. Starting at  $|E| = 1.8$  eV,  $O_1$  begins to drop sharply, meaning that most of these quasieigenstates exist in area II. Interestingly, here, the energy value  $|E| = 1.8$  eV corresponds exactly to the Van Hove singularities in the density of states of SC-pAA, which suggests that the energy corresponding to the Van Hove singularity is the distribution transition interval where the region occupied by eigenstates begins to change. Furthermore, as the pressure increases, the value of  $O_1$  becomes larger in the high-energy region and smaller in the low-energy region, resulting in a stronger localization of these states in corresponding energies. This means that greater pressure can cause the electrons to be distributed in the fractal-like space, i.e., area I. Near the Fermi level, we can see small peaks in  $O_1$  due to the boundary states at the top and bottom of area I in the SC-pAA sample [see Fig. 5(c)]. In Fig. 4(b), we can see similar behaviors of  $O_1$  in SC-pAB. Electrons are mainly distributed in area I inside the high-energy range. However, although  $O_1$  begins to drop sharply starting from the Van Hove singularity, the

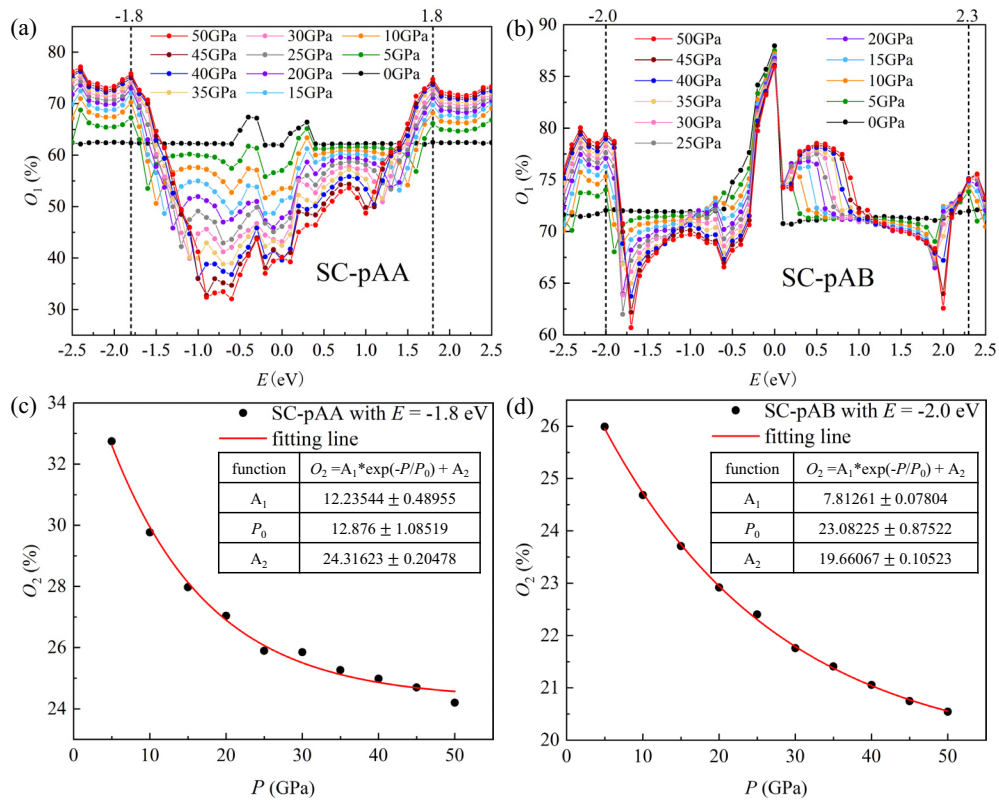


FIG. 4. (a) and (b) The occupation percentage  $O_1$  of area I in SC-pAA and SC-pAB under different pressures and energies. (c) and (d) The occupation percentage  $O_2$  of area II in SC-pAA and SC-pAB under different pressures at a single energy point ( $-1.8$  and  $-2.0$  eV). The sample parameters are set to  $W = 297.5a$  and  $I = 4$ .

percentage of occupation of  $O_1$  in area I remains above 60%, which means that electrons still occupy a relatively large proportion of the fractal space. The peak around the Fermi

energy  $E = 0$  eV represents the appearance of very strong boundary states in SC-pAB [see Fig. 5(g)], which is different from that in SC-pAA. We also plot the variation of  $O_2$  of area

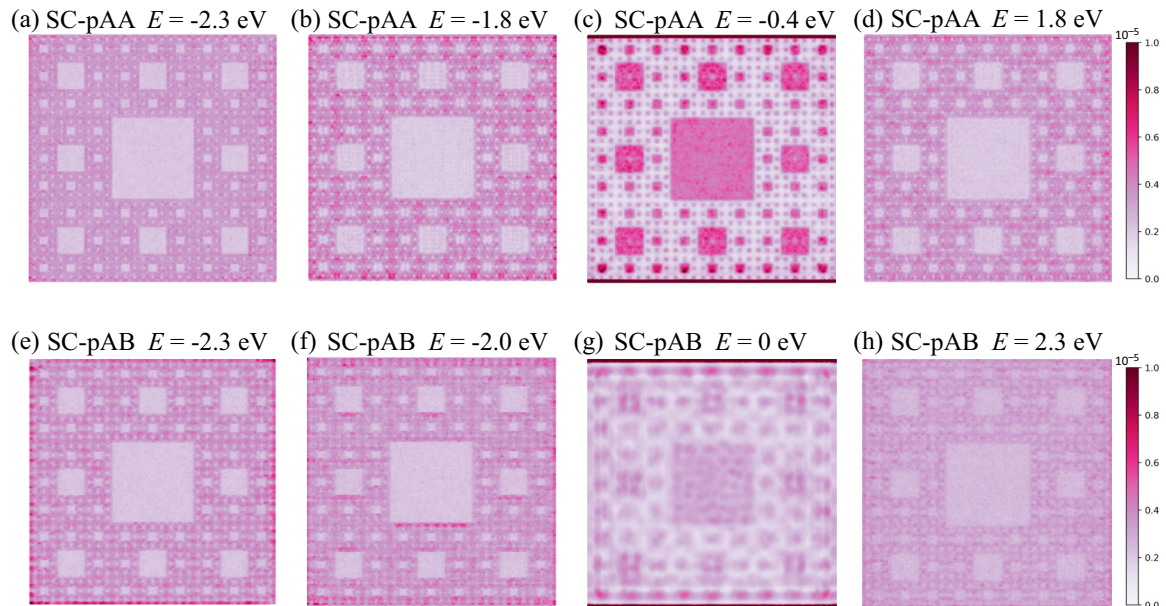


FIG. 5. The real-space distribution of quasieigenstates for SC-pAA at a pressure of 30 GPa at (a)  $E = -2.3$  eV, (b)  $E = -1.8$  eV, (c)  $E = -0.4$  eV, and (d)  $E = 1.8$  eV. The real-space distribution of quasieigenstates for SC-pAB at a pressure of 30 GPa at (a)  $E = -2.3$  eV, (b)  $E = -2.0$  eV, (c)  $E = 0$  eV, and (d)  $E = 2.3$  eV. The sample parameters are set to  $W = 297.5a$  and  $I = 4$ .

II under different pressures for a fixed energy in Figs. 4(c) and 4(d). Taking an energy near the Van Hove singularity as an example, the value of  $O_2$  varies with pressure in an exponential curve distribution. This means that as the pressure increases the change of  $O_2$  will gradually decrease.

For visualization, taking 30 GPa as an example, the real-space distributions of their quasieigenstates at several energies are shown in Fig. 5. For a high energy for SC-pAA in Fig. 5(a), the electrons are mainly distributed inside area I, suggesting that the electrons can be confined in fractal space. Even in the case of the transition energy, i.e., around the Van Hove singularity, the distribution remains in area I, as shown in Figs. 5(b) and 5(d). In contrast, for the low-energy region, we can see that the eigenstate is localized in area II in Fig. 5(c), and the localized boundary states at the top and bottom of the sample also manifest, which means that the electrons at the Fermi energy cannot enter the fractal space and are confined in the pressured region. Therefore, the pressure region cannot be regarded as vacancies in the low-energy region if the external pressure is infinite, and it is valid only in a high-energy region larger than the Van Hove singularities. A similar phenomenon also appears in SC-pAB, as shown in Figs. 5(e) and 5(f). At the Fermi energy, we can see these very strong boundary states at the top and bottom of the sample, and there is also a certain localization of electronic states in area II even though  $O_1$  is very large, as shown in Fig. 5(g). This also proves the central peak in Fig. 4(b). For the transition energy point of  $E = 2.3$  eV in Fig. 5(h), we can also see that the eigenstates are mainly distributed in area I, and the proportion of distribution in area II is not small.

Based on these results, we conclude that the distribution of quasieigenstates in SC-AA and SC-AB can confirm the energy broadening of central peaks in the energy spectrum increases. For fractal-like pressure-modulated bilayer graphene, the high-energy state localizes fractal space (area I) and can be regarded as vacancies if pressure is infinite. In the low-energy region, the electronic state of SC-pAB in area I still occupies a large proportion compared with that of SC-pAA, and the zero-energy position shows a very strong boundary state. Within a certain range, stronger pressure can lead to stronger localization, forming a more efficient fractal space.

### C. Quantum transport

In graphene SC systems, the geometry dimension can be revealed by the quantum conductance fluctuations by virtue of a box-counting (BC) method, i.e., the BC dimension of the quantum conductance fluctuations reflecting the Hausdorff dimension [10–12], which is the most prominent transport characteristic that other fractals do not have. However, for bilayer graphene fractals (SC-AA and SC-AB), the interlayer coupling may affect the quantum conductance fluctuations, and hence, it is meaningful to discuss whether the correlation between the BC dimension and the Hausdorff dimension still exists.

The calculation of quantum conductance is implemented in the KWANT software by the Landauer formula of the scattering theory. The numerical value of the conductance can be changed by the number, position, and width of the electrodes [10,11]. We discuss the quantum conductance under

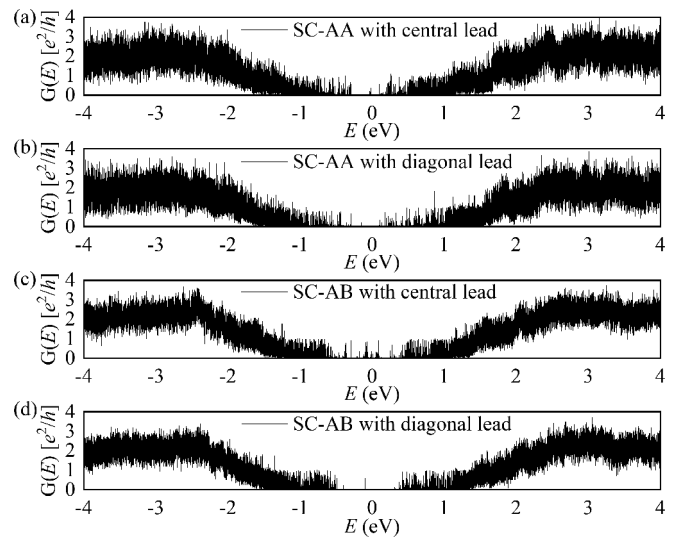


FIG. 6. The conductance  $G(E)$  (in units of  $e^2/h$ ) of (a) and (b) SC-AA and (c) and (d) SC-AB as a function of energy for central and diagonal lead positions, where lead width is  $4.15a$ . The sample parameters are set to  $I = 4$  and  $W = 297.5a$ .

two different lead position configurations, called the center leads (i.e., two leads are attached to the centers of the left and right sides of the sample) and the diagonal leads (i.e., one lead is attached to the bottom of one side and one lead is attached to the top of the other side), as shown in Fig. 1. The calculated quantum conductance spectra  $G(E)$  of SC-AA and SC-AB with different lead configurations are shown in Fig. 6. The conductance calculations for SC-pAA and SC-pAB are not performed since the matrix dimension in SC-pAA and SC-pAB exceed the computational limits of KWANT.

In monolayer graphene SCs, there is a remarkable conductance gap in the central part of  $G(E)$  where the conductance vanishes, which is a hallmark of electronic transport in SC fractals based on monolayer graphene [10–12]. However, in SC-AA and SC-AB based on bilayer graphene, several minor conductance peaks exist inside the low-energy region in Figs. 6(a)–6(c) because of the broadening of the central peaks near zero energy. The lead configurations also have remarkably different effects on the conductance inside the low-energy region. For the center lead case, the conductance gap almost vanishes, while a conductance gap exists, especially for SC-AB in Fig. 6(d) for the diagonal lead case.

Beyond the low-energy region, these conductance spectra contain many fluctuations, making the curve quite noisy. The fluctuations can be characterized by the dimension of the whole conductance spectrum, which can be obtained with the box-counting algorithm [68]. It is a pixel-based method, and the core of this algorithm is to cover the data points by boxes with a size  $r$ . The number of boxes  $N$  depends on the size of  $r$ , and when  $d = -\log_{10}(N)/\log_{10}(r)$  changes linearly, the value of  $d$  is called the BC dimension. In this situation,  $d$  is the slope of the function  $\log_{10} N[-\log_{10}(r)]$ , and the region where  $d$  change linearly is also called the scaling region. Actually, there are two other regions that have been dropped in the BC algorithm. For large values of  $r$ , where

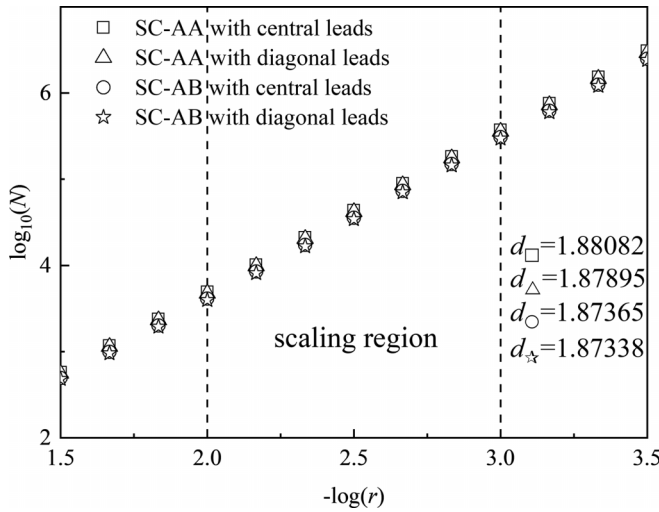


FIG. 7. Box-counting algorithm analysis of the conductance fluctuations for SC-AA and SC-AB in Fig. 6.

$-\log_{10}(r)$  is around zero, the box is too large to grasp the features of quantum conductance fluctuations, and for very small  $r$ , each box covers only one data point due to the very small size, so that  $N$  does not increase anymore and turns into a plateau. In Fig. 7, we show the numerical results for the BC algorithm for SC-AA and SC-AB. We consider the position effects of leads on the conductance spectrum and extract the BC dimension. For SC-AA (SC-AB), the values of the BC dimension are  $d_{\square} = 1.88082$  ( $d_{\triangle} = 1.87365$ ) and  $d_{\circ} = 1.87895$  ( $d_{\star} = 1.87338$ ) in the central and diagonal lead configurations, respectively. Surprisingly, the BC results in the SC based on bilayer graphene are very close to the Hausdorff dimension  $d_H = 1.89$ . We can further infer that the slight difference between the box-counting dimension and the Hausdorff dimension will vanish if the iteration number is infinite. This means that the correlation between quantum conductance and the geometry dimension remains in spite of the existing interlayer coupling in bilayer graphene SCs.

#### IV. SUMMARY

We investigated the DOS and quasieigenstates in SC-AA, SC-AB, SC-pAA, and SC-pAB structures and the quantum conductance fluctuations in SC-AA and SC-AB. The DOS results for SC-AA and SC-AB indicate larger energy broadening of the edge states compared with that of monolayer graphene SCs, and the DOS of SC-pAA (SC-pAB) in the high-energy region gradually become similar to that of SC-AA (SC-AB) as pressure increases, but it cannot exactly replicate the same spectrum as SC-AA (SC-AB) within the experimental pressure range. The analyses of real-space distributions of the normalized probability density for quasieigenstates also verified the DOS results. In SC-pAA, quasieigenstates around the zero energy are mainly localized inside area II, and the states inside the high-energy range are dispersed in fractal space (area I). In SC-pAB, the electronic state of area I in the low-energy region still occupies a large proportion compared with that of SC-pAA, and the zero-energy position shows a

very strong boundary state. By summing over the amplitudes of the normalized quasieigenstates in area I (i.e., occupation percentage), we found that within a certain pressure range, stronger pressure can lead to stronger localization, forming an efficient fractal space for high-energy quasieigenstates. We calculated the conductance spectrum in SC-AA and SC-AB and found that the quantum conductance fluctuations still follow the Hausdorff fractal dimension behavior. Thus, the high correlation between quantum conductance and the geometry dimension is not affected in bilayer graphene SCs in spite of the interlayer coupling. Based on this, it may be possible to characterize the geometric dimension of the graphene SC fractal experimentally by measuring the conductance in the future.

#### ACKNOWLEDGMENTS

This work was supported by the National Natural Science Foundation of China (Grants No. 12174291 and No. 12247101) and the Knowledge Innovation Program of the Wuhan Science and Technology Bureau (Grant No. 2022013301015171). Y.W. acknowledges the support from the 111 Project (Grant No. B20063) and the National Key Research and Development Program of China (Grant No. 2022YFA1402704). We thank the Core Facility of Wuhan University for providing the computational resources.

#### APPENDIX: TBPM

The TBPM is based on the numerical solution of the time-dependent Schrödinger equation (TDSE) with averaging over the random superposition of the basis states [61]. The numerical solution of the TDSE is carried out by using the Chebyshev polynomial algorithm. Taking the calculation of the DOS in Eq. (6) as an example, we show the detailed steps for the time-dependent evolution  $e^{-iHt}|\varphi(0)\rangle$  as follows.

Assuming  $x \in [-1, 1]$ ,  $e^{-izx}$  is expanded as

$$e^{-izx} = J_0(z) + 2 \sum_{m=1}^{\infty} (-i)^m J_m(z) T_m(x), \quad (\text{A1})$$

where  $J_m(z)$  is the Bessel function with order  $m$  and  $T_m(x) = \cos[m \arccos(x)]$  is the Chebyshev polynomial of the first kind.  $T_m(x)$  obeys the following recurrence relation:

$$T_{m+1}(x) + T_{m-1}(x) = 2xT_m(x). \quad (\text{A2})$$

As the Hamiltonian  $H$  has a complete set of eigenvectors  $|n\rangle$  with real-valued eigenvalues  $E_n$ , we can expand the wave function  $|\varphi(0)\rangle$  as a superposition of the eigenstates  $|n\rangle$ ,

$$|\varphi(0)\rangle = \sum_{n=1}^N |n\rangle \langle n|\varphi(0)\rangle, \quad (\text{A3})$$

and have

$$|\varphi(t)\rangle = e^{-itH}|\varphi(0)\rangle = \sum_{n=1}^N e^{-itE_n} |n\rangle \langle n|\varphi(0)\rangle. \quad (\text{A4})$$



Taking monolayer graphene as an example, with the nearest-neighbor hopping  $t$ , the next-neighbor hopping  $t'$ , and the on-site potential  $v$ , after using the inequality

$$\left\| \sum X_n \right\| \leq \sum \|X_n\|, \quad (\text{A5})$$

we find that

$$\|H\|_b \equiv 3t_{\max} + 6t'_{\max} + |v|_{\max} \geq \max\{E_n\}. \quad (\text{A6})$$

Introducing  $\hat{t} \equiv t\|H\|_b$  and  $\hat{E}_n \equiv E_n/\|H\|_b$ , where  $\hat{E}_n$  are the eigenvalues of a modified Hamiltonian  $\hat{H} \equiv H/\|H\|_b$ , we have

$$\hat{H}|E_n\rangle = \hat{E}_n|E_n\rangle. \quad (\text{A7})$$

By using Eq. (A1), the time evolution of  $|\varphi(t)\rangle$  can be represented as

$$|\varphi(t)\rangle = \left[ J_0(\hat{t})\hat{T}_0(\hat{H}) + 2 \sum_{m=1}^{\infty} J_m(\hat{t})\hat{T}_m(\hat{H}) \right] |\varphi(0)\rangle, \quad (\text{A8})$$

where the modified Chebyshev polynomial  $\hat{T}_m(\hat{E}_n)$  is

$$\hat{T}_m(\hat{E}_n) = (-i)^m T_m(\hat{E}_n), \quad (\text{A9})$$

which obeys the recurrence relation

$$\hat{T}_{m+1}(\hat{H})|\varphi\rangle = -2i\hat{H}\hat{T}_m(\hat{H})|\varphi\rangle + \hat{T}_{m-1}(\hat{H})|\varphi\rangle, \quad (\text{A10})$$

$$\hat{T}_0(\hat{H})|\varphi\rangle = I|\varphi\rangle, \quad (\text{A11})$$

$$\hat{T}_1\hat{H}|\varphi\rangle = -i\hat{H}|\varphi\rangle. \quad (\text{A12})$$

In this respect, we do not need to diagonalize the Hamiltonian matrix but do need to multiply the matrix repeatedly. The Chebyshev polynomial algorithm is very effective for simulating large systems. In addition, the Fourier transform in Eq. (6) is adopted by the fast Fourier transformation in TBPLAS, which greatly increases the computational efficiency.

- 
- [1] Y. Gefen, A. Aharony, and B. B. Mandelbrot, *J. Phys. A* **17**, 1277 (1984).
- [2] K. J. Falconer, *The Geometry of Fractal Sets* (Cambridge University Press, Cambridge, 1985).
- [3] L. Pietronero and E. Tosatti, *Fractals in Physics* (Elsevier, Amsterdam, 2012).
- [4] J. Feder, *Fractals* (Springer Science & Business Media, New York, 2013).
- [5] Q. Yao, X. Yang, A. A. Iliasov, M. I. Katsnelson, and S. Yuan, *Phys. Rev. B* **107**, 115424 (2023).
- [6] A. A. Iliasov, M. I. Katsnelson, and S. Yuan, *Phys. Rev. B* **102**, 075440 (2020).
- [7] A. A. Iliasov, M. I. Katsnelson, and S. Yuan, *Phys. Rev. B* **99**, 075402 (2019).
- [8] A. Kosior and K. Sacha, *Phys. Rev. B* **95**, 104206 (2017).
- [9] A. Hernando, M. Sulc, and J. Vanicek, [arXiv:1503.07741](https://arxiv.org/abs/1503.07741).
- [10] E. van Veen, S. Yuan, M. I. Katsnelson, M. Polini, and A. Tomadin, *Phys. Rev. B* **93**, 115428 (2016).
- [11] X. Yang, W. Zhou, P. Zhao, and S. Yuan, *Phys. Rev. B* **102**, 245425 (2020).
- [12] X. Yang, W. Zhou, Q. Yao, P. Lv, Y. Wang, and S. Yuan, *Phys. Rev. B* **105**, 205433 (2022).
- [13] A. A. Iliasov, M. I. Katsnelson, and S. Yuan, *Phys. Rev. B* **101**, 045413 (2020).
- [14] M. Fremling, M. van Hooft, C. M. Smith, and L. Fritz, *Phys. Rev. Res.* **2**, 013044 (2020).
- [15] G. Bouzerar and D. Mayou, *Phys. Rev. Res.* **2**, 033063 (2020).
- [16] Y.-L. Han and Z.-H. Qiao, *Front. Phys.* **14**, 63603 (2019).
- [17] T. Westerhout, E. van Veen, M. I. Katsnelson, and S. Yuan, *Phys. Rev. B* **97**, 205434 (2018).
- [18] A. Nandy, *Phys. Scr.* **96**, 045802 (2021).
- [19] A. Nandy, B. Pal, and A. Chakrabarti, *J. Phys.: Condens. Matter* **27**, 125501 (2015).
- [20] A. Nandy and A. Chakrabarti, *Phys. Lett. A* **379**, 2876 (2015).
- [21] B. Pal and K. Saha, *Phys. Rev. B* **97**, 195101 (2018).
- [22] S. Manna and B. Roy, *Commun. Phys.* **6**, 10 (2023).
- [23] S. Manna, S. Nandy, and B. Roy, *Phys. Rev. B* **105**, L201301 (2022).
- [24] M. N. Ivaki, I. Sahlberg, K. Pöyhönen, and T. Ojanen, *Commun. Phys.* **5**, 327 (2022).
- [25] S. Sarangi and A. E. B. Nielsen, *Phys. Rev. B* **104**, 045147 (2021).
- [26] S. Fischer, M. van Hooft, T. van der Meijden, C. M. Smith, L. Fritz, and M. Fremling, *Phys. Rev. Res.* **3**, 043103 (2021).
- [27] S. Manna, B. Pal, W. Wang, and A. E. B. Nielsen, *Phys. Rev. Res.* **2**, 023401 (2020).
- [28] S. Pai and A. Prem, *Phys. Rev. B* **100**, 155135 (2019).
- [29] M. Brzezińska, A. M. Cook, and T. Neupert, *Phys. Rev. B* **98**, 205116 (2018).
- [30] A. A. Iliasov, M. I. Katsnelson, and A. A. Bagrov, [arXiv:2310.11497](https://arxiv.org/abs/2310.11497).
- [31] Y. Zhou and P. Ye, [arXiv:2311.01199](https://arxiv.org/abs/2311.01199).
- [32] Z. Jiang *et al.*, *Angew. Chem., Int. Ed.* **56**, 11450 (2017).
- [33] D. Nieckarz and P. Szabelski, *Chem. Commun.* **52**, 11642 (2016).
- [34] X. Zhang *et al.*, *ACS Nano* **9**, 11909 (2015).
- [35] Q. Sun, L. Cai, H. Ma, C. Yuan, and W. Xu, *Chem. Commun.* **51**, 14164 (2015).
- [36] S. L. Tait, *Nat. Chem.* **7**, 370 (2015).
- [37] J. Shang, Y. Wang, M. Chen, J. Dai, X. Zhou, J. Kuttner, G. Hilt, X. Shao, J. M. Gottfried, and K. Wu, *Nat. Chem.* **7**, 389 (2015).
- [38] G. R. Newkome *et al.*, *Science* **312**, 1782 (2006).
- [39] X. Zhang, N. Li, L. Liu, G. Gu, C. Li, H. Tang, L. Peng, S. Hou, and Y. Wang, *Chem. Commun.* **52**, 10578 (2016).
- [40] N. Li, G. Gu, X. Zhang, D. Song, Y. Zhang, B. K. Teo, L.-m. Peng, S. Hou, and Y. Wang, *Chem. Commun.* **53**, 3469 (2017).
- [41] C. Liu, Y. Zhou, G. Wang, Y. Yin, C. Li, H. Huang, D. Guan, Y. Li, S. Wang, H. Zheng, C. Liu, Y. Han, J. W. Evans, F. Liu, and J. Jia, *Phys. Rev. Lett.* **126**, 176102 (2021).
- [42] H. Jiang *et al.*, *Sci. Bull.* **66**, 1312 (2021).
- [43] S. N. Kempkes, M. R. Slot, S. E. Freeney, S. J. Zevenhuizen, D. Vanmaekelbergh, I. Swart, and C. M. Smith, *Nat. Phys.* **15**, 127 (2019).

- [44] X.-Y. Xu, X.-W. Wang, D.-Y. Chen, C. M. Smith, and X.-M. Jin, *Nat. Photon.* **15**, 703 (2021).
- [45] L. Ge, K. Ni, X. Wu, Z. Fu, Y. Lu, and Y. Zhu, *Nanoscale* **13**, 9264 (2021).
- [46] B. L. Chittari, N. Leconte, S. Javvaji, and J. Jung, *Electron. Struct.* **1**, 015001 (2018).
- [47] M. Yankowitz, K. Watanabe, T. Taniguchi, P. San-Jose, and B. J. LeRoy, *Nat. Commun.* **7**, 13168 (2016).
- [48] J. E. Proctor, E. Gregoryanz, K. S. Novoselov, M. Lotya, J. N. Coleman, and M. P. Halsall, *Phys. Rev. B* **80**, 073408 (2009).
- [49] M. Yankowitz, J. Jung, E. Laksono, N. Leconte, B. L. Chittari, K. Watanabe, T. Taniguchi, S. Adam, D. Graf, and C. R. Dean, *Nature (London)* **557**, 404 (2018).
- [50] J. Nicolle, D. Machon, P. Poncharal, O. Pierre-Louis, and A. San-Miguel, *Nano Lett.* **11**, 3564 (2011).
- [51] D. Machon, C. Bousige, R. Alencar, A. Torres-Dias, F. Balima, J. Nicolle, G. de Sousa Pinheiro, A. G. Souza Filho, and A. San-Miguel, *J. Raman Spectrosc.* **49**, 121 (2018).
- [52] E. V. Castro, M. P. López-Sancho, and M. A. H. Vozmediano, *Phys. Rev. B* **84**, 075432 (2011).
- [53] X. Chen, S. Liu, J. N. Fry, and H.-P. Cheng, *J. Phys.: Condens. Matter* **34**, 385501 (2022).
- [54] D. Pant and R. Pati, *Nanoscale* **14**, 11945 (2022).
- [55] F. Sánchez-Ochoa, A. Rubio-Ponce, and F. López-Urías, *Phys. Rev. B* **107**, 045414 (2023).
- [56] B. Padhi and P. W. Phillips, *Phys. Rev. B* **99**, 205141 (2019).
- [57] M. Yankowitz, S. Chen, H. Polshyn, Y. Zhang, K. Watanabe, T. Taniguchi, D. Graf, A. F. Young, and C. R. Dean, *Science* **363**, 1059 (2019).
- [58] N. Marzari, A. A. Mostofi, J. R. Yates, I. Souza, and D. Vanderbilt, *Rev. Mod. Phys.* **84**, 1419 (2012).
- [59] S. Fang and E. Kaxiras, *Phys. Rev. B* **93**, 235153 (2016).
- [60] S. Carr, S. Fang, P. Jarillo-Herrero, and E. Kaxiras, *Phys. Rev. B* **98**, 085144 (2018).
- [61] S. Yuan, H. De Raedt, and M. I. Katsnelson, *Phys. Rev. B* **82**, 115448 (2010).
- [62] A. Hams and H. De Raedt, *Phys. Rev. E* **62**, 4365 (2000).
- [63] D. Kosloff and R. Kosloff, *J. Comput. Phys.* **52**, 35 (1983).
- [64] Y. Li, Z. Zhan, X. Kuang, Y. Li, and S. Yuan, *Comput. Phys. Commun.* **285**, 108632 (2023).
- [65] TBPLaS, <http://www.tbplas.net>.
- [66] C. W. Groth, M. Wimmer, A. R. Akhmerov, and X. Waintal, *New J. Phys.* **16**, 063065 (2014).
- [67] Z. Tao, J. Du, Z. Qi, K. Ni, S. Jiang, and Y. Zhu, *Appl. Phys. Lett.* **116**, 133101 (2020).
- [68] I. Guarneri and M. Terraneo, *Phys. Rev. E* **65**, 015203(R) (2001).